INTERNATIONAL JOURNAL FOR NUMERICAL METHODS IN FLUIDS
Int. J. Numer. Meth. Fluids 2002; **38**:533–553 (DOI: 10.1002/fld.227)

Numerical solution of the flow of thin viscous sheets under gravity and the inverse windscreen sagging problem

Roland Hunt*

Department of Mathematics, Strathclyde University, 26 Richmond Street, Glasgow G1 1XH, Scotland

SUMMARY

The slumping of a thin sheet of very viscous liquid glass is used in the manufacture of windscreens in the automotive industry. The governing equations for an asymptotically thin sheet with variable viscosity are derived in which the vertical coordinate forms the centre-line of the sheet. The time-dependant equations have been solved numerically using the backward Euler method to give results in both two and three dimensions. The flow of an initially flat sheet falls freely under gravity until it becomes curved and the flow becomes very slow in the 'slumped' phase. Finally the sheet freefalls as the thickness becomes small at the boundaries. The inverse problem in which the viscosity profile is to be determined for a given shape can be solved as an embedding problem in which a search is made amongst the forward solutions. Possible shapes in the two-dimensional problem are very restrictive and are shown to be related to the sheet thickness. In three dimensions the range of shapes is much greater.

KEY WORDS: thin viscous sheets; windscreen sagging problem

1. INTRODUCTION

There are many industrial processes involving the flow of viscous fluids such as fibres or thin sheets, and the solution of the Navier–Stokes equations characterised by free boundary conditions having large aspect ratios has attracted much interest both mathematically and numerically. For example, nearly one-dimensional viscous dominated fibres have been studied by Schultz and Davis [1] and Dewynne *et al.* [2–4]. In the same spirit thin sheets have been studied in which the governing equations have been derived as an asymptotic expansion via a parameter related to the sheet thickness. For example, thin sheets in two dimensions have been studied by Buckmaster *et al.* [5] and Wilmott [6] and a full non-linear model for the evolution of a three-dimensional sheet has been derived by Howell [7, 8] and applied to the blowing of a glass sheet [9]. Numerical solutions have been obtained using CFD codes [10, 11], for example Tuck *et al.* [12] uses finite elements to study the slumping of a liquid bridge under gravity.

* Correspondence to: R. Hunt, Department of Mathematics, Strathclyde University, 26 Richmond Street, Glasgow G1 1XH, Scotland.

Received 31 July 2000
Revised 24 May 2001

The problem of interest here is the so-called windscreen sagging problem. A two-dimensional thin sheet of molten glass of high viscosity is allowed to slump under the action of gravity. The coefficient of viscosity is variable depending on the temperature which is controlled by an array of lamps above the sheet. By suitably choosing the variation of temperature and hence viscosity the final shape of the sheet can be controlled. The process can be used in the manufacture of windscreens for the automobile industry.

The variation of a typical windscreen from a suitable reference plane is 5–20 per cent and it would appear possible to obtain a solution assuming that the vertical displacement referred to as the 'drop' is small (for example Howell [7]). However, a small drop analysis also assumes that the gradients are small but at the ends of the windscreen the gradient can be quite large. For this reason we will develop a model that allows for a drop of any magnitude. The governing equations developed in References [7–9] use a curvilinear coordinate system fixed in sheet using the normal and the tangential directions of the principle curvatures. These equations are difficult to solve numerically particularly at points where the principle curvatures are equal. For this reason we will derive the governing equations in a coordinate system more suitable for this particular problem. We use Cartesian coordinates x and y in a horizontal plane with vertical coordinate measured from the centre-line $z=H(x,y,t)$ defined such that the boundaries of the sheet are $H(x,y,t)\pm(1/2)h(x,y,t)$. This can be effected by performing Taylor expansions in the z-direction about the centre-line to all variables. The governing equations are then derived from the leading terms when applied to continuity and Navier–Stokes equations in which use of the kinematic and stress-free boundary conditions has been made.

For molten glass the viscosity μ varies considerably with temperature lying within a range 10^2–$10^8\,\mathrm{N\,s\,m^{-2}}$. A typical windscreen has dimensions $0.6\times1.5\,\mathrm{m}$ and we may set the length scale $L=1$. With density $\rho\sim2.5\times10^3\,\mathrm{kg\,m^{-3}}$ and acceleration due to gravity $g\sim9.8\,\mathrm{m\,s^{-2}}$ a typical slump velocity $V=gL^2\rho/\mu$ lies in the range 2.5×10^{-6}–2.5×10^2 with slump times L/V ranging from milliseconds to days, with hours being typical. The Reynolds number $Re=\rho VL/\mu=g\rho^2L^3/\mu^2$ lies in the range 6×10^{-9}–6×10^3 and hence we retain the inertia terms in the equation to accommodate the upper end of the range but for the most part this is not necessary. We have neglected surface tension since the capillary number $Ca=\mu V/\gamma=gL^2\rho/\gamma\sim10^5$ is large compared to unity where $\gamma=0.3\,\mathrm{N\,m^{-1}}$ is the coefficient of surface tension.

2. GOVERNING EQUATIONS

As in the introduction we suppose a thin sheet of fluid (Figure 1) has centre-line

$$z=H(x,y,t)$$

with vertical thickness $h(x,y,t)$ such that the boundaries of the sheet are

$$z=H\pm\tfrac{1}{2}h \tag{1}$$

Since the boundaries move with the fluid, a point $(x(t),y(t),z(t))$ lying in the surface will remain in the surface and satisfy Equation (1) at all times. Hence differentiating Equation (1) yields the kinematic boundary condition

$$H_t\pm\tfrac{1}{2}h_t+\mathbf{u}\cdot\mathbf{n}=0\quad\text{on } z=H\pm\tfrac{1}{2}h \tag{2}$$

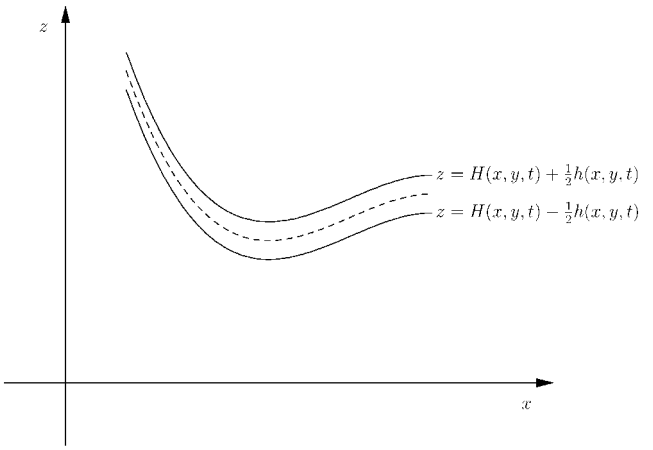

Figure 1. Geometry of the thin sheet with centre-line $z = H(x, y, t)$ (dotted) with boundaries $z = H(x, y, t) \pm (1/2)h(x, y, t)$ (solid).

where $\mathbf{u} = (u, v, w)$ is the fluid velocity, whose components will also be labelled u_i, $i = 1, 2, 3$ and $\mathbf{n}$ is the normal to a surface given by

$$\mathbf{n} = \mathbf{n}_0 \pm \tfrac{1}{2}\mathbf{n}_1$$

where $\mathbf{n}_0 = (H_x, H_y, -1)$ and $\mathbf{n}_1 = (h_x, h_y, 0)$ We will suppose that any dependent variable $\phi(x, y, z, t)$ can be written as a Taylor expansion in power of $(z - H)$ as

$$\phi = \phi_0 + (z - H)\phi_1 + \frac{1}{2!}(z - H)^2\phi_2 + O(z - H)^3$$

where ϕ_i depends only on (x, y, t). Regarding $\mathbf{n}_1$ as the next order smallness to $\mathbf{n}_0$ gives the leading two terms in Equation (2) as

$$H_t + \mathbf{u}_0 \cdot \mathbf{n}_0 = 0 \tag{3}$$

$$h_t + \mathbf{u}_0 \cdot \mathbf{n}_1 + h\mathbf{u}_1 \cdot \mathbf{n}_0 = 0 \tag{4}$$

The fluid flow is governed by the continuity and Navier–Stokes equations. The two leading terms of the continuity equation, $\nabla \cdot \mathbf{u} = 0$, give

$$\nabla \cdot \mathbf{u}_0 = \mathbf{u}_1 \cdot \mathbf{n}_0 \tag{5}$$

$$\nabla \cdot \mathbf{u}_1 = \mathbf{u}_2 \cdot \mathbf{n}_0 \tag{6}$$

where $\nabla = (\partial/\partial x, \partial/\partial y, \partial/\partial z)^T = (\partial/\partial x, \partial/\partial y, 0)^T$ since the operator will only be applied to variables which are independent of z. Combining Equations (4) and (5) gives

$$h_t + \nabla \cdot (h\mathbf{u}_0) = 0 \tag{7}$$

which is a conservation of mass statement regarding the sheet width h.

The Navier–Stokes equations can be written as

$$\frac{\partial \mathbf{u}}{\partial t} + (\mathbf{u} \cdot \nabla)\mathbf{u} = \frac{1}{\rho}\nabla \cdot \boldsymbol{\sigma} - \mathbf{g} \tag{8}$$

where $\boldsymbol{\sigma}$ is the stress tensor whose components are

$$\sigma_{ij} = -p\delta_{ij} + \mu(u_{i,j} + u_{j,i})$$

where $\mathbf{g} = (0, 0, g)$ and p is the pressure. The leading term of the expansion gives

$$\frac{\partial \mathbf{u}_0}{\partial t} + (\mathbf{u}_0 \cdot \nabla)\mathbf{u}_0 + \frac{1}{\rho}(\nabla p_0 - p_1 \mathbf{n}_0) = vD^2\mathbf{u}_0 + \mathbf{e}_0 \cdot \nabla v - (\mathbf{n}_0 \cdot \nabla v)\mathbf{u}_1 - (\mathbf{u}_1 \cdot \nabla v)\mathbf{n}_0 - \mathbf{g} \tag{9}$$

where use has been made of Equation (5) and

$$D^2\phi_0 = \phi_{0,xx} + \phi_{0,yy} - (H_{xx} + H_{yy})\phi_1 - 2(H_x\phi_{1,x} + H_y\phi_{1,y}) + (1 + H_x^2 + H_y^2)\phi_2$$

for any function ϕ_0 and $\mathbf{e}_q$ is a tensor related to the rate of strain tensor defined by

$$(\mathbf{e}_q)_{ij} = (\mathbf{u}_q)_{i,j} + (\mathbf{u}_q)_{j,i} \qquad q = 0, 1$$

It should be noted that the kinematic viscosity $v = \mu/\rho$ can depend on (x, y, t) but not on z; this will be used for the inverse problem.

The stress-free boundary condition $\boldsymbol{\sigma} \cdot \mathbf{n} = 0$ is applied to both boundaries. The leading two terms of the expansion are

$$\boldsymbol{\sigma}_0 \cdot \mathbf{n}_0 = 0 \tag{10}$$

$$\boldsymbol{\sigma}_0 \cdot \mathbf{n}_1 + h\boldsymbol{\sigma}_1 \cdot \mathbf{n}_0 = 0 \tag{11}$$

where the various terms can be evaluated using

$$\boldsymbol{\sigma}_q \cdot \mathbf{n}_r = -p_q\mathbf{n}_r + \mu[\mathbf{e}_q \cdot \mathbf{n}_r - (\mathbf{u}_{q+1} \cdot \mathbf{n}_r)\mathbf{n}_0 - (\mathbf{n}_0 \cdot \mathbf{n}_r)\mathbf{u}_{q+1}] \quad q = 0, 1 \quad r = 0, 1 - q$$

Equations (3)–(6) and (9)–(11) form a set of 13 equations for the unknowns $\mathbf{u}_0, \mathbf{u}_1, \mathbf{u}_2$, p_0, p_1, H and h and are the minimum required to obtain a leading order solution. Variables $\mathbf{u}_1$ and p_0 appear in Equations (5) and (10) linearly and undifferentiated. Hence we can find expressions for these variables using matrix inversion. Substituting the formulae for these into Equations (6) and (11) we similarly observe that the variables $\mathbf{u}_2$ and p_1 appear linearly and undifferentiated and can be found by matrix inversion. The expressions for these variables were found using Maple [13] are not presented here due to their inordinate length. Substitution of these four variables into the remaining Equations (3), (4) and (9) form a set of time dependent equations of the form

$$\frac{\partial \mathbf{U}}{\partial t} = \mathbf{F}(\mathbf{U}) \tag{12}$$

where $\mathbf{U} = (\mathbf{u}_0, H, h)$ which needs to be solved numerically. These equations govern the solution in the limit as $h \to 0$ and hence the value of h is evaluated relative to some nominal thickness, for example, its value initially. In all our calculations we suppose h is given at $t = 0$.

3. NUMERICAL SOLUTION IN TWO DIMENSIONS

In this section we will suppose that we have no y dependence. The governing equations can be obtained from Section 2 by setting the velocity $v=0$ and $\partial/\partial y=0$. For convenience the vertical direction is relabelled as y and the vertical velocity as v. We consider the problem in which the sheet is fixed at two points $x=\pm L,\ y=0$ and is initially flat with constant thickness. The equations are non-dimensionalised using L as the unit of length, $U=\sqrt{gL}$ as the unit of velocity and ρU^2 as the unit of stress which give equations similar to the original equations with $g=L=\rho=1$. The time-dependent Equations (3), (4) and (9) are

$$\begin{aligned} u_{0,t} &= -u_0 u_{0,x} - \tilde{p}_{0,x} + vD^2 u_0 + 2\tilde{u}_{0,x} v_x \\ u_{0,t} &= -u_0 v_{0,x} - p_1 + vD^2 v_0 + (u_{0,y} + \tilde{v}_{0,x}) v_x - 1 \\ H_t &= v_0 - u_0 H_x \\ G_t &= -u_{0,x} - u_0 G_x \end{aligned} \tag{13}$$

where

$$\begin{aligned} \tilde{\phi}_{i,x} &= \phi_{i,x} - H_x \phi_{i+1} \\ D^2\phi_0 &= \phi_{0,xx} - H_{xx}\phi_1 - 2H_x\phi_{1,x} + (1+H_x^2)\phi_2 \end{aligned}$$

for any variable ϕ and $i=0,1$ and $1/v$ acts as a Reynolds number. Here we have introduced $G=\ln h$ which ensures that h always remains positive in the numerical calculation. These four equations govern the evolution of $\mathbf{U}=(u_0, v_0, H, G)$ and the other variables are found algebraically as previously indicated. Specifically the resulting formulae are

$$p_0 = -2vA_0J, \quad u_1 = B_0J^2, \quad v_1 = C_0J^2 \tag{14}$$

$$p_1 = -2vA_1J, \quad u_2 = (B_1 + 4G_xA_0J)J^2, \quad v_2 = (C_1 + 4G_xH_xA_0J)J^2 \tag{15}$$

where

$$\begin{aligned} A_i &= u_{i,x} + H_x v_{i,x}, \quad i=0,1 \\ B_i &= H_x(H_x^2+3)u_{i,x} + (H_x^2-1)v_{i,x}, \quad i=0,1 \\ C_i &= (H_x^2-1)(u_{i,x} + H_x v_{i,x}), \quad i=0,1 \\ J &= (1+H_x^2)^{-1} \end{aligned}$$

Equations (13), (14) and (15) completely specify the problem which is solved numerically as follows.

The problem is symmetric about $x=0$ and hence we seek a solution on the domain $0\leqslant x\leqslant 1$. An equally spaced grid, $x_i=i\Delta x,\ i=0,1,\ldots,N$, is placed on the domain where $\Delta x=1/N$ is the mesh width and $\mathbf{U}_i^n$ is an approximation for $\mathbf{U}$ at x_i for time level n. Since Equations (14)

and (15) only involve first derivatives it is convenient to locate p_0, u_1 and v_1 at the staggered (1/2)-integer locations and to approximate the derivatives, for any ϕ, by

$$\phi_{,x}|_{i+1/2} = \frac{\phi_{i+1} - \phi_i}{\Delta x}, \quad \text{and} \quad \phi_{,x}|_i = \frac{\phi_{i+1/2} - \phi_{i-1/2}}{\Delta x} \tag{16}$$

where the first of these is used in Equation (14) and the second in Equation (15). Hence if $\mathbf{U}_i^n$, $i = 0, 1, \ldots, N$ is known at any stage of the calculation then p_0, u_1, v_1, p_1, u_2 and v_2 can be found at all the grid points for this time level using Equations (14), (15) and (16). The derivatives on the right side of Equation (13) are approximated using standard second order central differences given by

$$\phi_{,x}|_i = \frac{\phi_{i+1} - \phi_{i-1}}{2\Delta x}, \quad \text{and} \quad \phi_{,xx}|_{i,j} = \frac{\phi_{i+1} - 2\phi_i + \phi_{i-1}}{\Delta x^2}$$

the exception being $p_{0,x}$ for which we use the second of Equation (16). Occasionally the value of a variable is required at an integer location which is held at a (1/2)-integer point. For this we use a simple average

$$\phi_i = \frac{1}{2}(\phi_{1+1/2} + \phi_{i-1/2}) \tag{17}$$

Equation (13) is of the form of Equation (12) where the right hand side is now algebraic. The time derivatives are approximated by first order backward differences and the numerical method for Equation (12) is

$$\mathbf{U}_i^{n+1} = \mathbf{U}_i^n + \Delta t \mathbf{F}_i^{n+1} \tag{18}$$

where and Δt is the time-step. Hence the time advance employs the backward Euler method which has very good stability characteristics. At the left hand boundary, $i = 0$, the solution is symmetric and we introduce a fictitious node at $i = -1$ and apply the appropriate symmetric boundary conditions. At the right hand boundary, $i = N$, the sheet is fixed giving $u_0 = v_0 = H = 0$ and G is updated using the fourth of Equation (13) with one-sided differences to approximate the x-derivatives. Equation (18) and these boundary conditions form a set of non-linear equations at each time level which is solved using Newton's method.

As will become evident in the next section, there are periods of very rapid movement at the beginning and end of the flow, with a period, in between, of very slow, 'slumped' flow. In order to accommodate this, a variable time-step is used such that the local error estimate T is always less than some prescibed tolerance ε throughout the calculation. Specifically at each time-step we calculate

$$\begin{aligned}
\mathbf{U}_i^{n+1} &= \mathbf{U}_i^n + \Delta t \mathbf{F}_i^{n+1} \\
\mathbf{V}_i^{n+1/2} &= \mathbf{V}_i^n + \tfrac{1}{2}\Delta t \mathbf{F}_i^{n+1/2} \\
\mathbf{V}_i^{n+1} &= \mathbf{V}_{i+1/2}^n + \tfrac{1}{2}\Delta t \mathbf{F}_i^{n+1} \\
\tilde{\mathbf{V}}_i^{n+1} &= \mathbf{V}_i^n + \Delta t \mathbf{F}_i^{n+1}
\end{aligned}$$

Since the backward Euler method is first order, we use $T = \max_i |\tilde{\mathbf{V}}_i^{n+1} - \mathbf{V}_i^{n+1}|$ to estimate the local error, which is used to control the value of Δt in the usual way. For the case $v = 100$,

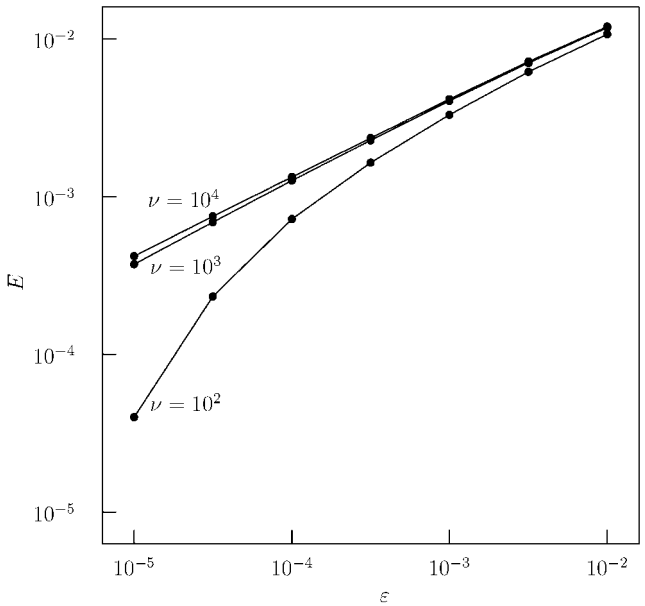

Figure 2. RMS error estimates E in the 'slumped' flow as a function of the tolerance ε for various values of v.

the value of Δt ranges from 0.01 in the rapid regions to 10 in the 'slumped' region. After each time-step $\mathbf{V}_i^{n+1}$ is the required result, being more accurate than $\mathbf{U}_i^{n+1}$. Again noting that the method is first order the RMS error in $\mathbf{V}_i^{n+1}$ at each time level is given by

$$E = \frac{1}{4N} \sum_i |\mathbf{V}_i^{n+1} - \mathbf{U}_i^{n+1}|$$

Figure 2 shows the maximum value of E in the 'slumped' region as a function of the tolerance ε when $N=128$ for three values of v. The diagram clearly shows that the results converge as $\varepsilon \to 0$, and that a tolerance of 10^{-4} is sufficient to give results having error of about 10^{-3}. In order to estimate the error incurred in the x-direction, results with $N=32$, 64, 128 and 256 having the same Δt at each time-step were compared. It was evident that setting $N=128$ is adequate for a tolerance of 10^{-3}.

4. RESULTS FOR THE TWO-DIMENSIONAL PROBLEM

Using the numerical procedure, results have been obtained for constant viscosity with $v = 10^{\alpha}$, $\alpha = -2, -1, \ldots, 6$ which covers the range for molten glass. These are illustrated in Figures 3–10 for $v = 100$ and show that the flow passes through three distinct phases. In the first phase the horizontal flat profile falls under gravity with the flat sections being unaffected by the viscosity. The contours of H are shown in Figure 3 for $t = 0.0(0.05)0.4$ in which the flat section is gradually eroded and disappears at about $t = 0.4$. The corresponding vertical velocities v_0 are

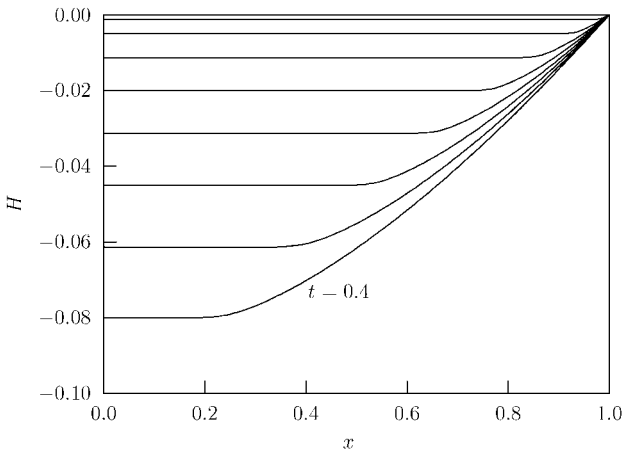

Figure 3. Profiles of H for $t = 0(0.05)0.4$.

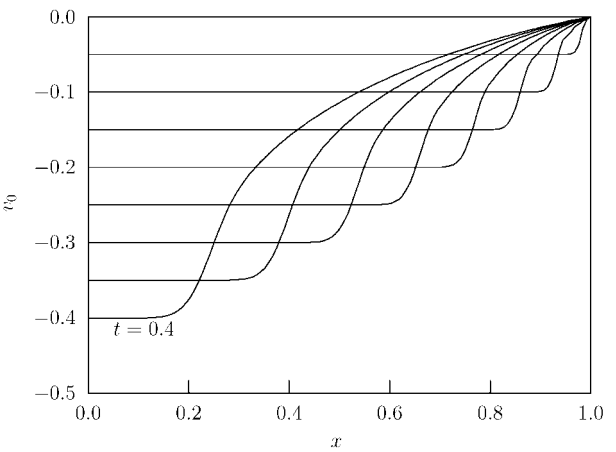

Figure 4. Profiles of v_0 for $t = 0(0.05)0.4$.

shown in Figure 4 with the central velocity increasing linearly. After $t = 0.4$ the magnitude of v_0 gradually decreases (Figure 5) passing through a period of 'sloshing' oscillations until it settles down to a velocity with a shallow parabolic like profile by about $t = 40$. The weak damping in these osciallations is shown in Figure 6 which shows the central velocity $v_0(0, t)$ as a function of t. For $t > 40$ the flow has now entered the second phase which is the 'slumped' flow. Here viscous forces dominate and the sheet gradually falls with a minimum central vertical velocity ~ -0.005 at about $t = 90$. Figure 7 shows the normal thickness $h/\sqrt{1 + H'^2}$ as a fraction of the initial thickness. Initially this thickness is unchanged, as has been shown analytically in the shallow solution case [7], but as time passes the thickness decreases which

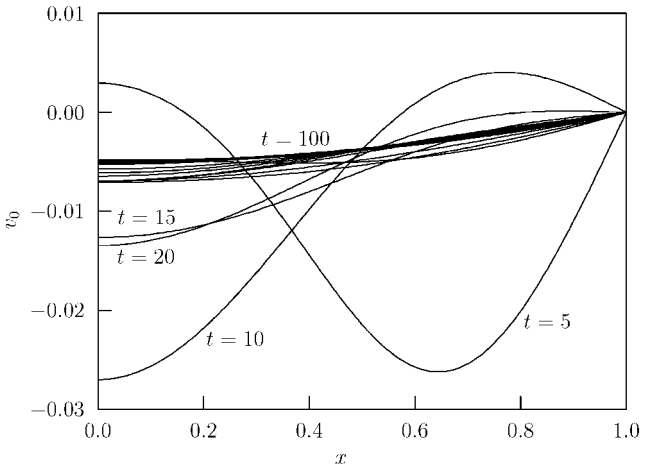

Figure 5. Profiles of v_0 for $t = 5(5)100$.

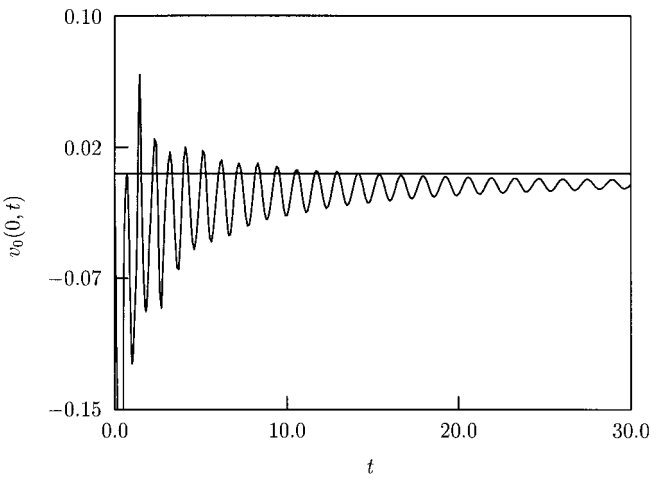

Figure 6. Variation of $v_0(0,t)$ with time t.

is a consequence of mass being conserved. This occurs principly at the edges with the result that the 'slump' velocity gradually increases (Figure 8). At about $t = 300$ the thickness at the edges is so small that bulk of the sheet starts to fall under gravity. The flow now enters the third phase in which the sheet is virtually disconnected from its supports. Now the flow is again freefalling with the thickness of the edge $\to 0$ as $t \to 355.4$. Figure 9 shows the variation of H over the whole time span clearly showing the rapid drops in the first and third phases and the 'slumping' flow of the second phase. The horizontal velocity u_0 is substantially less than v_0 by at least an order of magnitude with some profiles shown in Figure 10.

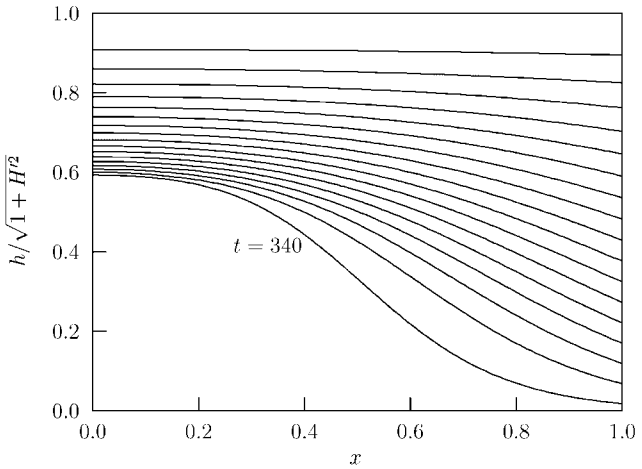

Figure 7. Profiles of h for $t = 0(20)340$.

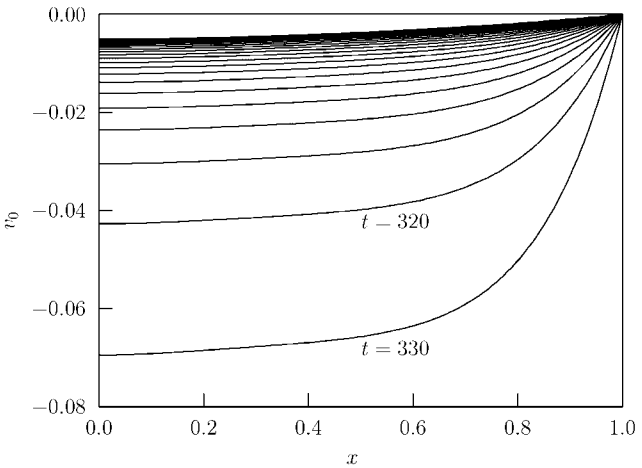

Figure 8. Profiles of v_0 for $t = 100(10)330$.

The above description is typical for $v \geqslant 10$, however for $v = 1$ the 'slumping' phase is very short and non-existant for $v < 1$. This is can be seen in Figure 11 which shows the central drop as a function of the time t for each value of α. The parabola shows the freefall path of the initial phase from which the curves break away when entering the 'slumping' phase. For large v the times involved are large and it is more convenient to scale time with $1/\lambda$. Figure 12 shows the drop H plotted against t/v. The curves for $v \geqslant 100$ virtually coincide and are indistinguishable in the diagram with $v = 10$ very close to these. The slow drop of the 'slumping' phase is clearly shown followed by the rapid descent of the final free-fall.

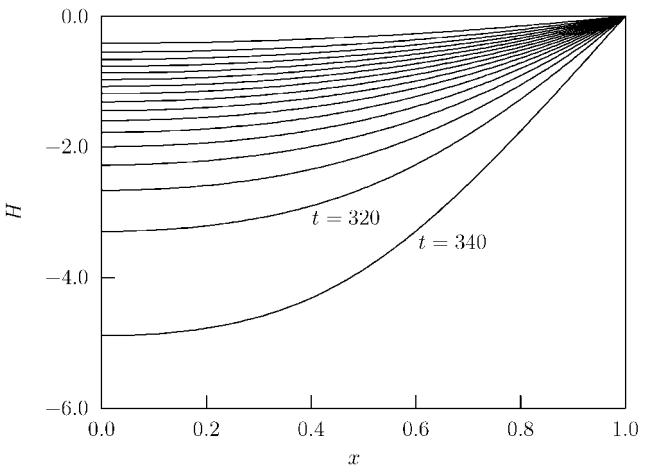

Figure 9. Profiles of H for $t = 0(20)340$.

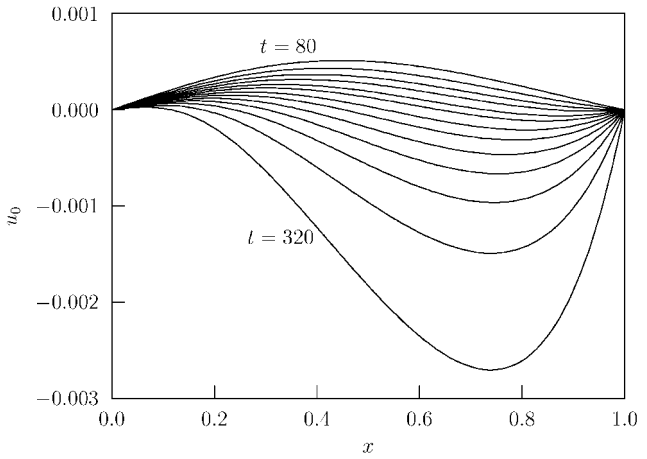

Figure 10. Profiles of u_0 for $t = 80(20)320$.

5. NUMERICAL SOLUTION IN THREE DIMENSIONS

We consider the case where the sheet is fixed on the boundaries of a rectangle $x = \pm M$, $y = \pm L$ at $z = 0$. The problem is non-dimensionalised as previously with L as the unit of length and then the boundary will be $x = \pm a$, $y = \pm 1$ where $a = M/L$ is the aspect ratio and we may assume $a \geqslant 1$ without loss of generality. Formulae for p_0, p_1, $\mathbf{u}_1$ and $\mathbf{u}_2$ were calculated using Maple similar to Equations (14) and (15) and converted directing into Fortran which ensures they are error free. The variables p_0 and $\mathbf{u}_1$ are held at the $(1/2)$-integer points which are the cell centres of a grid placed on the rectangle with mesh spacing $\Delta x = a/N_x$ and $\Delta y = 1/N_y$ where $N_x \times N_y$ is the size of the grid. The discretisations for the derivatives are similar to

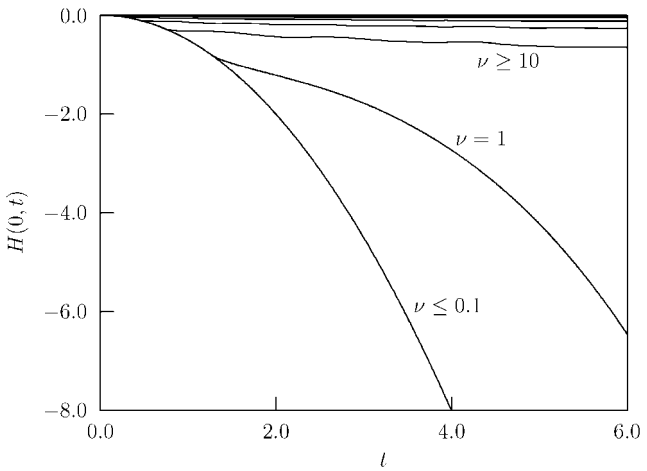

Figure 11. Plot of $H(0)$ as a function of t for $v = 10^{\alpha}$, $\alpha = -2, -1, \ldots, 6$.

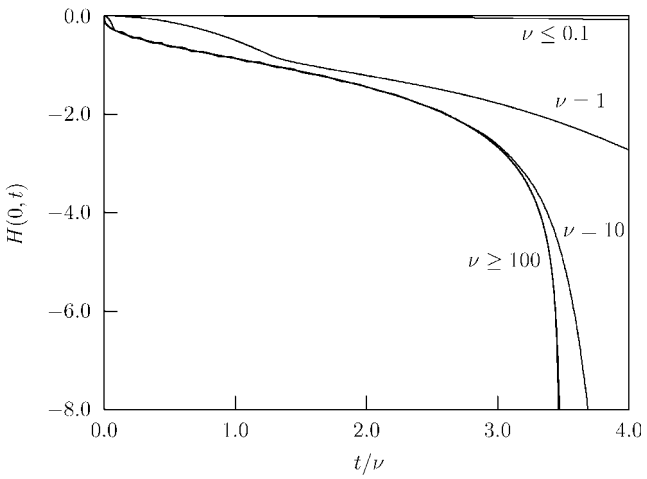

Figure 12. Plot of $H(0)$ as a function of t/v for $v = 10^{\alpha}$, $\alpha = -2, -1, \ldots, 6$.

those of the previous section. Some derivatives involve averaging, for example, the derivatives at cell centres, corresponding to Equation (16) become

$$\phi_{,x}|_{i+1/2,j+1/2} = \frac{\phi_{i+1,j+1} + \phi_{i+1,j} - \phi_{i,j+1} - \phi_{i,j}}{2\Delta x}$$

$$\phi_{,x}|_{i,j} = \frac{\phi_{i+1/2,j+1/2} + \phi_{i+1/2,j-1/2} - \phi_{i-1/2,j+1/2} - \phi_{i-1/2,j-1/2}}{2\Delta x}$$

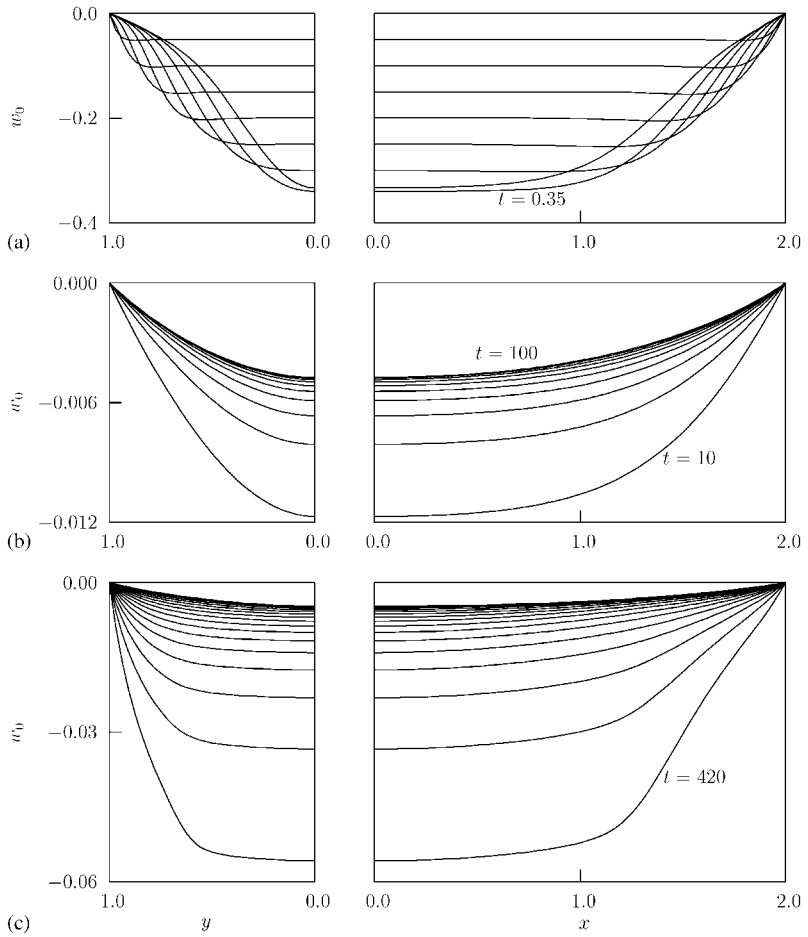

Figure 13. Profiles of v_0 for (a) $t = 0(0.05)0.4$ (b) $t = 10(10)100$ and (c) $t = 100(20)420$.

with similar expressions for the y derivatives, and the averaging of Equation (17) involves the four nearest neighbours

$$\phi_{i,j} = \tfrac{1}{4}(\phi_{1+1/2,j+1/2} + \phi_{i+1/2,j-1/2} + \phi_{i-1/2,j+1/2} + \phi_{i-1/2,j-1/2})$$

The time advance of the vector $\mathbf{U} = (\mathbf{u}_0, H, G)$ uses exactly the same technique as outlined in Section 3.

Results for the three-dimensional flow have very similar characteristics to those observed in the two-dimensional case and will be illustrated for $v = 100$ only. The results for an aspect ratio $a = 2$ and using a 32×64 grid are depicted in Figures 13 and 14 which show the centre-line profiles of the five variables, the left hand graph in the plane $x = 0$ and the right-hand graph in $y = 0$. As in the two-dimensional case the flow passes through the same three phases. Figure 13(a) shows the profiles of vertical velocity w_0 for times up to $t = 0.4$ of the first phase in which the sheet falls under gravity until it is arrested by viscous stresses as

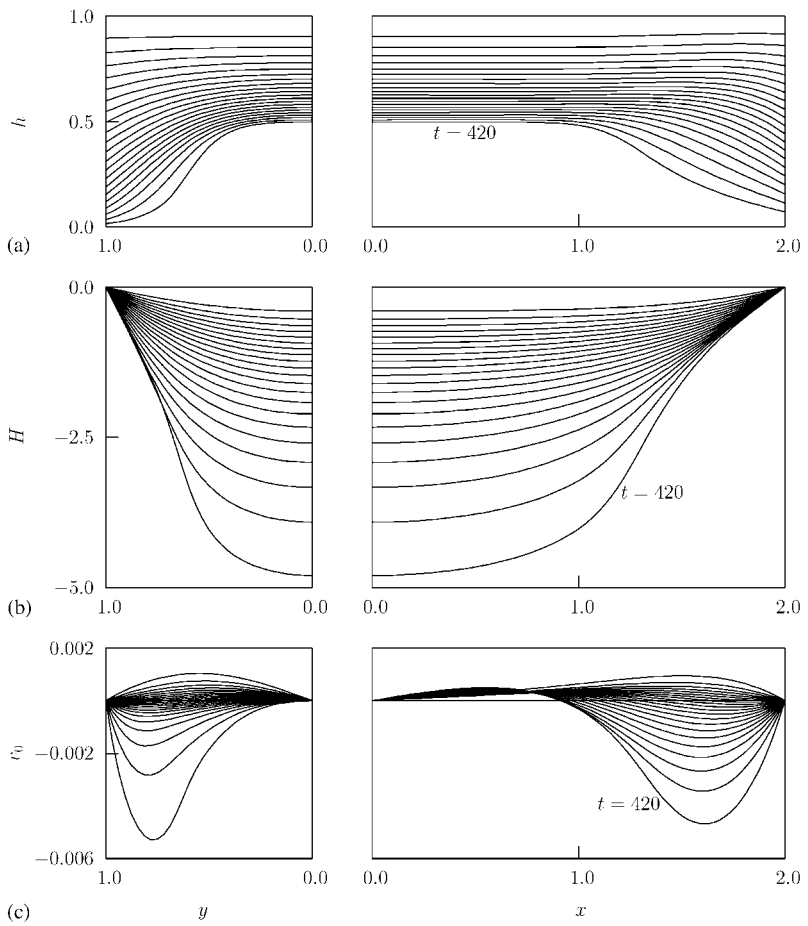

Figure 14. Profiles for $t = 0(20)420$ of (a) h (b) H and (c) u_0.

the sheet becomes curved, the central velocity reaching a maximum magnitude of 0.343 at $t = 0.37$. After this the central velocity magnitude decreases as shown in Figure 13(b) and we enter the 'slump' phase reaching a minimum value of 0.0047 at about $t = 100$. The flow remains in the slumped phase until the sheet thickness becomes thin at the edges as shown in Figure 14(a) occuring first in the longer of the two sides. The flow then enters the final phase with the bulk of the sheet falling under gravity with vertical velocity profiles as shown in Figure 13(c). The profiles of the centre-line H of the sheet are shown in Figure 14(b) for equally spaced times showing rapid movement for early and late times and a slower movement during intermediate times. Finally Figure 14(c) shows the centre-line velocity profiles for u_0 in the right-hand graph and v_0 on the left. A comparison of Figures 13 and 14 with Figures 3–10 shows that the two- and three-dimensional flows are characteristically very similar. Figure 15 shows profiles of H for various aspect ratios a. As a increases the time taken to reach a given depth decreases since the boundaries at $x = \pm a$ have diminishing effect on the flow. This is shown clearly in the insert which plots H at the centre point (0,0) as a function of t.

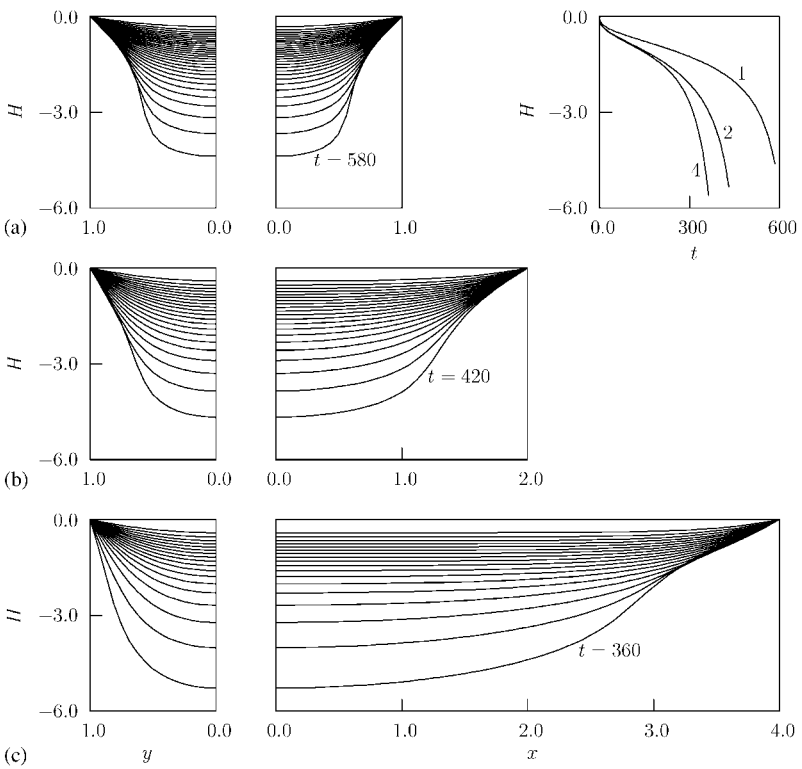

Figure 15. Profiles for H for $t = 0, 20, 40, \ldots$ with aspect ratio (a) 1 (b) 2 and (c) 4. The insert shows the position of the centre point against t.

6. THE INVERSE PROBLEM

So far we have considered the case in which the viscosity profile, usually constant, is specified and the resultant shape of the sheet, given by $H(x, y, t)$ is obtained for various times t. The industrial problem of interest is the reverse of this, namely, given a centre-line profile, $\bar{H}(x, y)$, what is the viscosity profile $v(x, y)$ which will produce this drop after some time T, where T is sufficiently large to ensure we are in the slumped phase.

The method consists of searching amongst the forward solutions until a viscosity profile $v(x, y)$ is found which gives the required solution $\bar{H}(x, y)$ to within a prescribed tolerance. For simplicity we will describe the technique for the two-dimensional case, the extension to three dimensions is straightforward. Thus we will search amongst the various $v(x)$ until $\|H(x, T) - \bar{H}(x)\| < \varepsilon$ where ε is a prescribed tolerance. The number of forward solutions that are required is quite prohibitive and to keep the problem manageable we will approximate $v(x)$ and $\bar{H}(x)$ by orthonormal even polynomials p_i and q_i of degree $2i$, $i = 0, 1, 2, \ldots$ defined as

$$\int_0^1 p_i(x)\, p_j(x)\, \mathrm{d}x = \delta_{ij} \qquad \int_0^1 (1 - x^2) q_i(x) q_j(x)\, \mathrm{d}x = \delta_{ij} \tag{19}$$

then

$$v(x) \simeq \sum_{i=0}^{m} a_i p_i(x) \quad \bar{H}(x) \simeq (1-x^2) \sum_{i=0}^{m} b_i q_i(x) \tag{20}$$

where

$$a_i = \int_0^1 v(x) p_i(x)\,\mathrm{d}x \quad b_i = \int_0^1 \bar{H}(x) q_i(x)\,\mathrm{d}x \tag{21}$$

for the coefficients a_i and b_i. The integrals in Equation (21) are performed numerically using the grid values with the trapezoidal rule. If the polynomials p_i and q_i in Equation (19) are defined using the trapezoidal rule with the same grid points rather than analytically, then the errors in $v(x)$ and $\bar{H}(x)$ in Equation (20) decrease spectrally. The multiplicative factor outside the summation in the second of Equation (20) and the weight in the second of Equation (19) take advantage of the boundary condition that H and $\bar{H}$ are zero on the boundary, which makes for a more accurate approximation for given m. For given a_i we can calculate $v(x)$ using the first of Equation (20) and then numerically calculate $H(x,T)$ which can be expressed in the form of the second of Equation (20) with coefficients c_i where

$$c_i = \int_0^1 H(x,T) q_i(x)\,\mathrm{d}x$$

Hence the inverse problem consists of choosing the a_i such that $c_i = b_i$ for $i = 0, 1, \ldots, m$, which is accomplished using Newton's method as follows. We can regard the c_i as functions of a_i and are required to solve

$$\begin{aligned} c_0(a_0, a_1, \ldots, a_m) &= b_0 \\ c_1(a_0, a_1, \ldots, a_m) &= b_1 \\ &\vdots \\ c_m(a_0, a_1, \ldots, a_m) &= b_m \end{aligned}$$

that is

$$\mathbf{c}(\mathbf{a}^T) = \mathbf{b} \tag{22}$$

where $\mathbf{a}, \mathbf{b}$ and $\mathbf{c}$ are the vectors of the coefficients having length $(m+1)$. Then Newton's method is

$$\begin{aligned} \mathbf{a}^{(s+1)} &= \mathbf{a}^{(s)} + \Delta\mathbf{a}^{(s)} \\ J\Delta\mathbf{a}^{(s)} &= \mathbf{b} - \mathbf{c}^{(s)} \end{aligned} \qquad s = 0, 1, 2, \ldots$$

where $\mathbf{c}^{(s)}$ are the coefficients obtained when $\mathbf{a} = \mathbf{a}^{(s)}$ and J is the Jacobian matrix whose (i,j)th element is $\partial c_i / \partial a_j$. The elements of J need to be calculated numerically and we use the formula

$$\frac{\partial c_i}{\partial a_j} \simeq \frac{1}{\varepsilon} \left[c_i(a_0^{(s)}, \ldots, a_j^{(s)} + \varepsilon, \ldots, a_m^{(s)}) - c_i(a_0^{(s)}, \ldots, a_j^{(s)}, \ldots, a_m^{(s)}) \right] \tag{23}$$

where ε is small but not too small (10^{-3} was used in the calculations). Hence in addition to calculating the solution for $\mathbf{a}^{(s)}$ we need a further $(m+1)$ calculations to find the solution

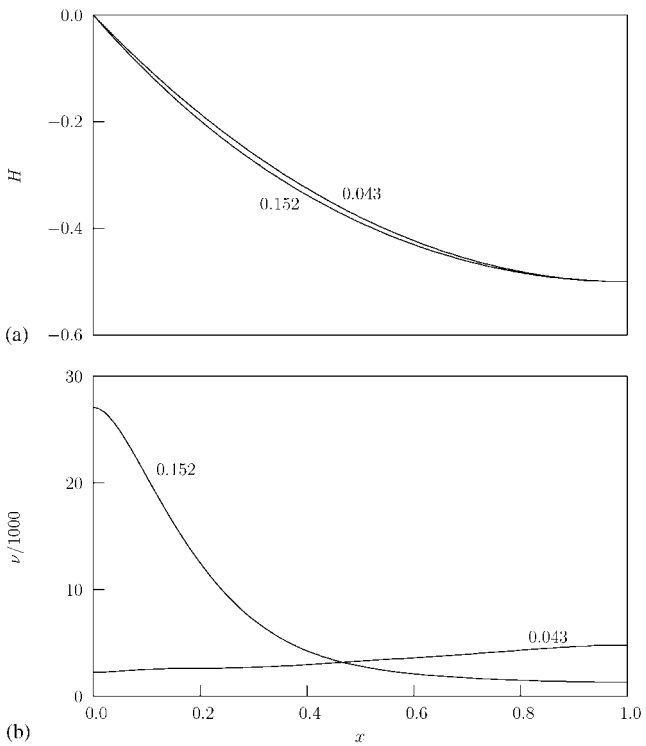

Figure 16. Profiles of (a) $\bar{H}$ and (b) v for the limiting values of B when $A = 0.5$.

for $(a_0^{(s)}, \ldots, a_j^{(s)} + \varepsilon, \ldots, a_m^{(s)})$, $j = 0, 1, \ldots, m$ which can be costly. However, the value of m is quite small since we only require the approximations in Equation (20) to lie within the tolerance ε and setting $\varepsilon = 10^{-3}$ it was found that $m = 6$ is usually sufficent. In the slump phase the required viscosity $v(x)$ is proportional to T and hence we may use any large value for T and, in practice, we set $T = 1000$.

To illustrate the technique we have chosen

$$\bar{H}(x) = -A(1 - x^2)(1 + Bx^2) \tag{24}$$

with $A = 0.5$ and $A = 1$ for a range of values of B. For $A = 0.5$ results were obtained for B in the range $0.043 \leqslant B \leqslant 0.152$ and for values of B outside this range no numerical solution could be obtained and it is likely that in this case no solution exists. Profiles for $\bar{H}(x)$ and $v(x)$ at the limits of this range are shown in Figure 16. The possible profiles for $\bar{H}(x)$ are very restrictive and are very close to the shape produced by a constant viscosity. The corresponding two viscosity profiles are very different in both shape and magnitude and show that a small change in $\bar{H}(x)$ produces a large change in $v(x)$. The situation for $A=1$ is slightly more promising with a range of $0.000 \leqslant B \leqslant 0.880$ for B and the profiles for the limiting values are shown in Figure 17.

To see why the possible profiles are so restrictive we can make some progress analytically. In the slump region the inertial terms can be neglected and Equation (8) becomes the non-

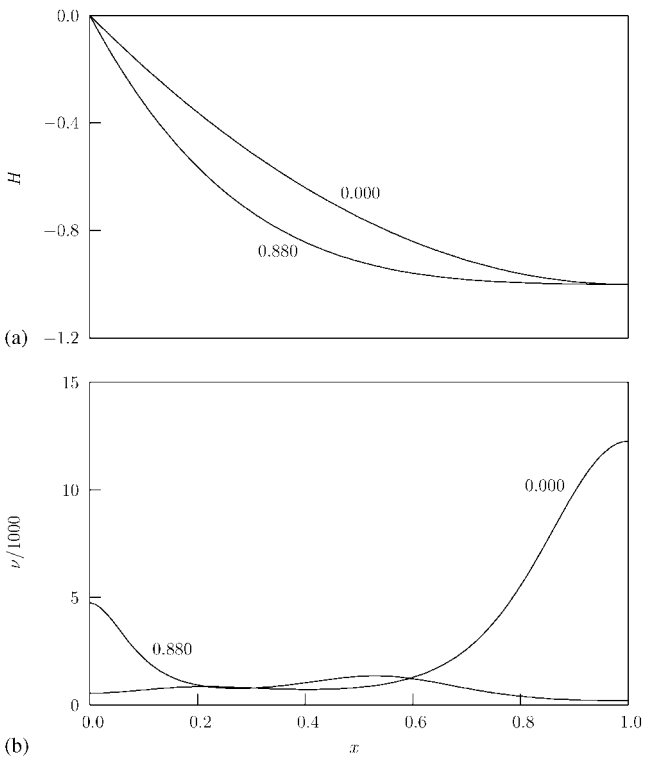

Figure 17. Profiles of (a) $\bar{H}$ and (b) v for the limiting values of B when $A = 1$.

dimensional Stokes equation $\nabla \cdot \boldsymbol{\sigma} = \mathbf{e}_y$ which in component form is

$$\frac{\partial}{\partial x}\sigma_{xx} + \frac{\partial}{\partial y}\sigma_{xy} = 0$$
$$\frac{\partial}{\partial x}\sigma_{xy} + \frac{\partial}{\partial y}\sigma_{yy} = 1$$

which give the leading term in the expansion as

$$\frac{\partial}{\partial x}\sigma_{0xx} - H_x\,\sigma_{1xx} + \sigma_{1xy} = 0$$
$$\frac{\partial}{\partial x}\sigma_{0xy} - H_x\,\sigma_{1xy} + \sigma_{1yy} = 1$$

Using the free stress boundary conditions of Equations (10) and (11) these reduce to

$$\frac{1}{h}\frac{\partial}{\partial x}(h\sigma_{0xx}) = 0 \qquad \frac{1}{h}\frac{\partial}{\partial x}(hH_x\,\sigma_{0xx}) = 1$$

From the first of these we observe that $h\sigma_{0xx}$ depends on t alone. Setting $h\sigma_{0xx} = 1/f(t)$ for some function f, the second equation yields

$$H_{xx} = hf(t) \tag{25}$$

Thus the shape of the centre-line profile depends only on h. The continuity Equation (7)

$$\frac{\partial h}{\partial t} + \frac{\partial}{\partial x}(hu_0) = 0$$

governs the variation in h which depends on u_0. In the slump phase the velocity is principally vertical with $v_0 \gg u_0$ and hence the variation in h is slight. When h is a constant the shape of the centre-line profile is necessarily parabolic and since $H = 0$ at $x = \pm 1$ we have

$$H = -\tfrac{1}{2}(1 - x^2)hgf(t)$$

with shape $R = 1 - x^2$. Obtaining profiles significantly different from this is at best difficult and at worst impossible since no solution will exist.

For the three-dimensional problem, however, the above analysis does not give the simple solution that the shape of H depends solely on h since there is no equivalent solution similar to Equation (25). Because of this the range of solutions of the inverse problem in three dimensions is much less restrictive. As described earlier we suppose that the fixed boundaries of the sheet are $x = \pm a$ and $y = \pm 1$ with symmetry about $x = 0$ and $y = 0$. The polynomials p_i and q_i are as defined in Equation (21) previously and we express $v(x, y)$ and $\bar{H}(x, y)$ by

$$\begin{aligned} v(x, y) &\simeq \sum_{i=0}^{k} \sum_{j=0}^{i} a_{ij}\, p_i(x/a)\, p_j(y) \\ \bar{H}(x, y) &\simeq (a^2 - x^2)(1 - y^2) \sum_{i=0}^{k} \sum_{j=0}^{i} b_{ij} q_i(x/a) q_j(y) \end{aligned} \tag{26}$$

where

$$\begin{aligned} a_{ij} &= \frac{1}{a} \int_0^a \int_0^1 v(x, y)\, p_i(x/a)\, p_j(j)\, \mathrm{d}x\, \mathrm{d}y \\ b_{ij} &= \frac{1}{a^3} \int_0^a \int_0^1 \bar{H}(x, y) q_i(x/a) q_j(y)\, \mathrm{d}x\, \mathrm{d}y \end{aligned} \tag{27}$$

for $i = 0, 1, \ldots, k,\ j = 0, 1, \ldots, i$, that is for all non-negative i and j satisfying $i + j \leqslant k$.

As in the two-dimensional case, for given a_{ij} we can calculate $v(x, y)$ using the first of Equation (26) and then numerically calculate $H(x, y, T)$ from which we find the c_{ij} using

$$c_{ij} = \frac{1}{a^3} \int_0^a \int_0^1 H(x, y, T) q_i(x/a) q_j(y)\, \mathrm{d}x\, \mathrm{d}y$$

Hence, as before, the inverse problem consists of choosing the a_{ij} such that $c_{ij} = b_{ij}$ for all i and j and can be written as Equation (22) with $m = (1/2)k(k + 3)$.

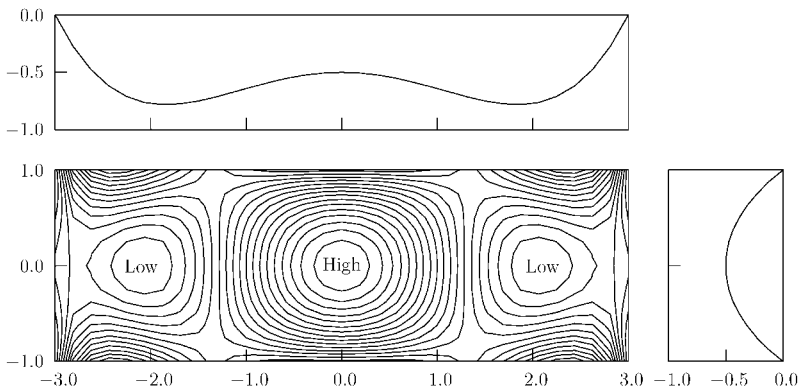

Figure 18. Contour plot of v which gives a drop $\bar{H}$ as given by Equation (28). The center-line profiles of $\bar{H}$ are shown above and to the right. v has a maximum of 2.664×10^4 (indicated by the 'High') and a minimum of 2.783×10^2 (indicated by the 'Low') with contour heights increasing by a factor 1.2563.

We illustrate with

$$\bar{H}(x, y) = -A(a^2 - x^2)(1 - y^2)(1 + Bx^2 + Cy^2 + Dx^2 y^2) \tag{28}$$

with aspect ratio $a = 3$ and $A = 1/18$, $B = 4$, $C = 0.1$ and $D = BC$. This has centre-line profiles as shown in Figure 18 and is clearly different from the constant viscosity results described earlier. Results for the viscosity $v(x, y)$ were obtained with $m = 20$ (using $k = 5$) and is shown as a contour map in Figure 18.

7. CONCLUSION

The governing equations for the time dependant motion of a thin sheet under the influence of gravity have been derived and solved numerically for both constant and variable viscosity in two and three dimensions. The solution for the sheet that has reasonably large viscosity and is initially flat show that the evolution passes through three distinct phases. Firstly the sheet drops under gravity with negligilbe viscous forces away from the boundaries. Secondly, as the sheet becomes curved, viscous forces dominate and the sheet 'slumps' with small velocities. Finally at the boundaries the sheet becomes so thin that it is no longer supportable by the edges and free falls.

The inclusion of variable viscosity allows the solution of the inverse problem, that is, to calculate the viscosity profile that produces a prescribed drop. In two dimensions we found it was not possible to obtain solutions for problems whose centre-line profiles are significantly different from those produced by a constant viscosity. Analysis of the governing equations reveals that the shape of the centre-line profile is governed by the sheet thickness whose variation is often only slight. In three dimensions the situation is more promising and has been illustrated with a single example.

For the production of car windscreens the frame used as the boundary will not usually be rectangular or lie in a plane. Further, the glass sheet is often dropped or thrown onto the

frame and hence the inital condition will not be static. Both of these extensions form the basis of possible future work.

REFERENCES

1. Schultz WW, Davis SH. One-dimensional liquid fibers. *Journal of Rheology* 1982; **26**:331–345.
2. Dewynne JN, Ockendon JR, Wilmott P. On a mathematical model for fibre tapering. *SIAM Journal of Applied Maths* 1989; **49**:983–990.
3. Dewynne JN, Ockendon JR, Wilmott P. Systematic derivation of the leading-order equations for extensional flows in slender geometries. *Journal of Fluid Mechanics* 1992; **224**:323–338.
4. Dewynne JN, Howell PD, Wilmott P. Slender viscous fibres with inertia and gravity. *Quarterly Journal of Mechanics and Applied Mathematics* 1994; **47**:541–555.
5. Buckmaster JD, Nachman A, Ting L. The buckling and stetching of a viscida. *Journal of Fluid Mechanics* 1975; **69**:1–20.
6. Wilmott P. The stetching of a thin viscous inculsion and the drawing of glass sheets. *Physics of Fluids A* 1989; **7**:1098–1103.
7. Howell PD. Extensional thin layer flows. D. Phil. Thesis, University of Oxford, 1994.
8. Howell PD. Models for slender thin viscous sheets. *European Journal of Applied Mathematics* 1996; **7**:321–343.
9. van de Fliert BW, Howell PD, Ockendon JR. Pressure-driven flow of a thin viscous sheet. *Journal of Fluid Mechanics* 1995; **292**:359–376.
10. Burley DM, Graham SJ. The blowing of thin films into moulds with applications in the glass container industry. *Mathematics of Finite Elements and Applications* 1991; **7**:279–286.
11. Graham SJ, Burley DM, Carling JC. Fluid flow in thin films using finite elements. *Mathematical Engineering in Industry* 1992; **3**:229–246.
12. Tuck EO, Stokes YM, Schwarz LW. Slow slumping of a very viscous bridge. *Journal of Engineering Mathematics* 1997; **32**:27–40.
13. Char BW, Geddes KO, Gonnet GH, Leong BL, Monagan MB, Watt SM. *First Leaves: A Tutorial Introduction to Maple V*. Springer-Verlag, Berlin, 1992.

